Exceptional degeneracies in non-Hermitian Rashba semiconductors

OPEN ACCESS
IOP Publishing
Journal of Physics: Condensed Matter
J. Phys.: Condens. Matter **35** (2023) 254002 (10pp)
https://doi.org/10.1088/1361-648X/acc7e9

Exceptional degeneracies in non-Hermitian Rashba semiconductors

Jorge Cayao

Department of Physics and Astronomy, Uppsala University, Box 516, S-75120 Uppsala, Sweden

E-mail: jorge.cayao@physics.uu.se

Received 12 January 2023, revised 6 March 2023
Accepted for publication 27 March 2023
Published 6 April 2023

Abstract

Exceptional points (EPs) are spectral degeneracies of non-Hermitian (NH) systems where eigenvalues and eigenvectors coalesce, inducing unique topological phases that have no counterpart in the Hermitian realm. Here we consider an NH system by coupling a two-dimensional semiconductor with Rashba spin–orbit coupling (SOC) to a ferromagnet lead and show the emergence of highly tunable EPs along rings in momentum space. Interestingly, these exceptional degeneracies are the endpoints of lines formed by the eigenvalue coalescence at finite real energy, resembling the bulk Fermi arcs commonly defined at zero real energy. We then show that an in-plane Zeeman field provides a way to control these exceptional degeneracies although higher values of non-Hermiticity are required in contrast to the zero Zeeman field regime. Furthermore, we find that the spin projections also coalescence at the exceptional degeneracies and can acquire larger values than in the Hermitian regime. Finally, we demonstrate that the exceptional degeneracies induce large spectral weights, which can be used as a signature for their detection. Our results thus reveal the potential of systems with Rashba SOC for realizing NH bulk phenomena.

Keywords: non-Hermitian semiconductor, open semiconductor, material junction, Rashba spin–orbit coupling, exceptional points

(Some figures may appear in colour only in the online journal)

1. Introduction

The effect of dissipation, often seen as detrimental, has recently attracted a paramount attention in physics due its potential to induce novel phenomena with technological applications [1–7]. Dissipation naturally occurs in open systems and is effectively described by non-Hermitian (NH) Hamiltonians [8–10]. The most salient property of these NH models is the emergence of a complex spectrum with degeneracies known as exceptional points (EPs) [11–21], where eigenstates and eigenvalues coalesce, in stark contrast to Hermitian systems. While EPs were initially seen as a mathematical curiosity, it has been recently shown that they represent truly topological objects enabling topological phases with no counterpart in Hermitian setups [3, 4, 7].

The concept of EPs and their topological properties have recently been generalized to higher dimensions, giving rise to exceptional degeneracies in the form of lines, rings, and surfaces as generic and stable bulk phenomena. These exceptional degeneracies have already proven crucial to enable unique topological effects [3, 4], such as enhanced sensing [22, 23], unidirectional lasing [24, 25], and bulk Fermi arcs [26–38], which do not have a Hermitian analog. Despite the numerous theoretical and experimental studies, however, the majority

of them has investigated exceptional degeneracies mostly in optical and photonic systems [1, 2, 5, 6].

Material junctions have been shown to offer another powerful and experimentally relevant platform for the realization of exceptional degeneracies [39–47]. Material junctions constitute electronic open systems with a clear NH description that is well-established in quantum transport [48]. In this regard, open semiconductor-superconductor junctions have been shown to host several classes of exceptional degeneracies [41, 42, 47], which characterize distinct NH topological phases without analog in the Hermitian regime. Notwithstanding the importance of this study, it only focused on the impact of non-Hermiticity on the superconducting properties, such as on its particle-hole symmetry and energy gap, leaving largely unexplored the role of non-Hermiticity on the semiconductor. Of particular importance in such semiconductors is their intrinsic Rashba spin–orbit coupling (SOC) [49–51], which arises due to the lack of structural inversion symmetry and induces a spin-momentum locking [52, 53]. This property of the Rashba SOC has been shown to enable a great control of the electron's spin, a crucial ingredient for several spintronics and topological phenomena [54], already proven useful in recent experiments [53–58]. However, despite the advances, the interplay between Rashba SOC and non-Hermiticity still remains unknown, specially the potential of this combination for inducing exceptional degeneracies.

In this work we consider a realistic NH Rashba semiconductor and discover the formation of stable and highly tunable bulk exceptional degeneracies. In particular, we engineer an NH Rashba system by coupling a two-dimensional (2D) semiconductor with Rashba SOC to a semi-infinite ferromagnet lead, an easily achievable heterostructure using e.g. InAs or InSb semiconductors [53–58], see also [59]. We discover that EPs appear along rings in 2D momentum space and mark the ends of lines formed by the coalescence of eigenvalues at finite real energy. The emergence of eigenvalues at the same real energy resembles the formation of bulk Fermi arcs, which, although initially conceived at zero real energy, have recently been generalized to finite real energies [60]. We also show that the exceptional degeneracies found here can be controlled by an in-plane Zeeman field but then higher values of non-Hermiticity are required. Furthermore, we find that the spin projections coalesce at the exceptional degeneracies and can even develop larger values than in the Hermitian phase due to non-Hermiticity. Finally, we find that the exceptional degeneracies induce large spectral features, which can be detected, e.g. using angle-resolved photoemission spectroscopy (ARPES).

2. NH effective model

We consider an open system by coupling a 2D semiconductor with Rashba SOC to a semi-infinite ferromagnet lead, as schematically shown in figure 1. This open system is modeled by the following effective NH Hamiltonian

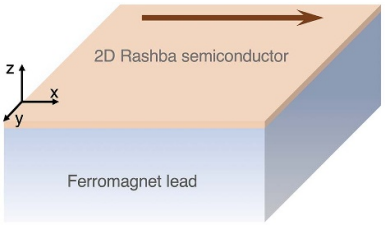

Figure 1. Schematics of studied non-Hermitian Rashba system: a 2D Rashba semiconductor (orange) is coupled to a semi-infinite ferromagnet lead (gray). A Zeeman field along x is applied (brown) in order to control the emergent non-Hermitian degeneracies.

$$H_{\rm eff} = H_{\rm R} + \Sigma^r(\omega = 0)\,, \tag{1}$$

where $H_{\rm R}$ describes the closed system, which is Hermitian, and $\Sigma^r(\omega = 0)$ is the zero-frequency retarded self-energy due to the coupling to the semi-infinite ferromagnet lead. More specifically, the closed system corresponds to a 2D Rashba semiconductor described by

$$H_{\rm R} = \xi_k + \alpha(k_y\sigma_x - k_x\sigma_y)\,, \tag{2}$$

where $\xi_k = \hbar^2(k_x^2 + k_y^2)/2m - \mu$ is the kinetic energy, $k_{x(y)}$ the momentum along $x(y)$, μ is the chemical potential, α is the Rashba SOC strength, and σ_j the jth Pauli matrix in spin space, and without loss of generality we assume $\hbar = m = 1$. The Hamiltonian $H_{\rm R}$ in equation (2) describes well the Rashba SOC in 2D semiconductors, such as in InAs or InSb, which are also within experimental reach [53–59]. As an external control knob, we also consider that the closed system is subjected to an applied magnetic field along x which produces a Zeeman field B, denoted by the brown arrow in figure 1. The effect of this Zeeman field is modeled by adding $B\sigma_x$ to $H_{\rm R}$ in equation (2) which induces a renormalization to the SOC term $\alpha k_y\sigma_x$.

The zero-frequency self-energy $\Sigma^r(\omega = 0)$ in equation (1), whose independence of frequency ω is well justified in the wide-band limit [48], is analytically obtained and given by [45, 46]

$$\Sigma^r(\omega = 0) = -i\Gamma\sigma_0 - i\gamma\sigma_z\,, \tag{3}$$

where $\Gamma = (\Gamma_\uparrow + \Gamma_\downarrow)/2$ and $\gamma = (\Gamma_\uparrow - \Gamma_\downarrow)/2$, with $\Gamma_\sigma = \pi|t'|^2\rho_{\rm L}^\sigma$, being t' the hopping amplitude into the lead from the 2D Rashba semiconductor and $\rho_{\rm L}^\sigma$ the surface density of states of the lead for spin $\sigma = \uparrow, \downarrow$. It is thus evident that Γ_σ characterizes the coupling amplitude between the lead and the 2D Rashba semiconductor. For completeness, the derivation of the self-energy given by equation (3) is presented in appendix.

The self-energy in equation (3) is imaginary and thus NH, a unique effect emerging due to the coupling to the semi-infinite ferromagnet lead. Thus, the imaginary self-energy renders the total effective Hamiltonian $H_{\rm eff}$ to be NH, introducing dramatic changes in the properties of the closed system $H_{\rm R}$, which is the focus of this work here. In particular, we are interested in investigating the interplay between non-Hermiticity

and Rashba SOC in 2D semiconductors and how it leads to the formation of bulk exceptional degeneracies.

3. Exceptional degeneracies

To identify the emergence of bulk exceptional degeneracies, we obtain the eigenvalues and eigenvectors of the effective Hamiltonian $H_{\rm eff}$ given by equation (1). At zero Zeeman field $B=0$, they are given by

$$E_{\pm} = \xi_k - i\Gamma \pm \sqrt{\alpha^2|k|^2 - \gamma^2}\,, \tag{4}$$

$$\Psi_{\pm} = \frac{1}{\sqrt{2}}\begin{pmatrix} 1 \\ \frac{i\gamma \pm \sqrt{\alpha^2|k|^2-\gamma^2}}{\alpha(k_y+ik_x)} \end{pmatrix}, \tag{5}$$

where $|k|^2 = k_x^2 + k_y^2$ and $\pm$ labels the two distinct bands which have a mixture of $\uparrow$ and $\downarrow$ spins. At finite Zeeman fields B, the eigenvalues and eigenvectors can be obtained by replacing $\alpha k_y \to B + \alpha k_y$ in equations (4) and (5). An immediate observation in the energies and wavefunctions is their dependence on the couplings $\Gamma_{\uparrow,\downarrow}$ via γ and Γ, already revealing a clear impact of the NH self energy given by equation (3). This can be visualized in figure 2, where we plot the eigenvalues and eigenvectors as a function of momenta k_x and k_y at zero Zeeman field. At $\Gamma_{\uparrow,\downarrow}=0$, the system described by equation (1) is Hermitian and its two eigenvalues in equation (4) are real: they correspond to two parabolas shifted by $\pm k_{\rm soc} = \pm m\alpha/\hbar^2$ that intersect at $k_{x,y}=0$, see gray curves in figure 2(a). Here, their respective eigenvectors are orthogonal as expected for Hermitian systems, see equation (5). While this Rashba system is gapless at zero momenta, finite values of k_y opens a gap at $k_x=0$ even at zero Zeeman field. A finite in-plane Zeeman field opens a gap at $k_{x,y}=0$, also known as helical gap, where states are counter propagating and have distinct spins [59, 61–63].

At any $\Gamma_{\uparrow,\downarrow}\neq 0$, the two eigenvalues $E_{\pm}$ acquire finite imaginary parts that strongly depend on momenta, see equation (4). The formation of eigenvalues with imaginary terms signals the emergence of NH physics as a pure effect due to the ferromagnet lead [45–47]. The inverse of these imaginary parts define the quasiparticle lifetime in the 2D Rashba semiconductor, thus offering a clear physical meaning of non-Hermiticity [48]. From the dependence of the eigenvalues on γ in equation (4), we note that their imaginary parts exhibit a non trivial behavior. In fact, at $\gamma=0$, which is satisfied when $\Gamma_{\uparrow}=\Gamma_{\downarrow}$, the two eigenvalues acquire the same imaginary part equal to $-i\Gamma$. This situation remains for $\gamma\neq 0$ only when $|\gamma|<\alpha|k|$. At these conditions, therefore, quasiparticles in the Rashba semiconductor have the same and constant lifetime.

The behavior of the eigenvalues becomes more interesting when $\gamma\neq 0$ and $|\gamma|>\alpha|k|$, which then allows the two eigenvalues to acquire distinct imaginary parts. This is visualized in figure 2(a) where we plot the real and imaginary parts of the

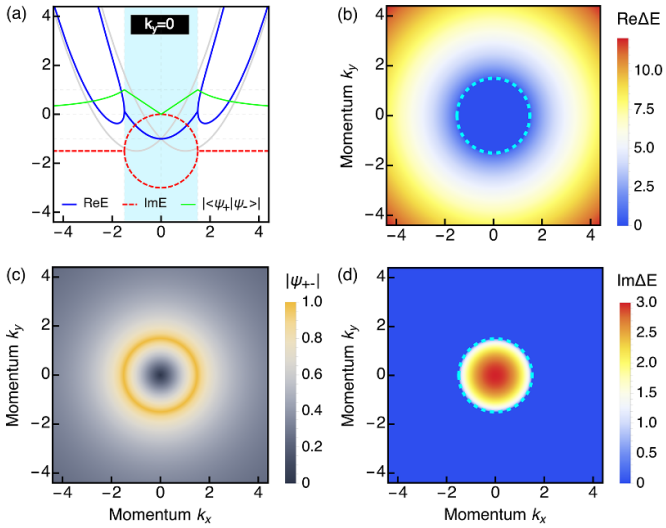

Figure 2. Exceptional degeneracies in 2D Rashba semiconductors at zero Zeeman field: (a) Real (Re) and imaginary (Im) parts of the eigenvalues as a function of k_x depicted in solid blue and dashed red curves at $k_y=0$. Green curve represents the absolute value of the overlap between the two wavefunctions $\psi_{+-}=\langle\psi_+|\psi_-\rangle$. Gray curves show eigenvalues without non-Hermiticity, $\Gamma_{\uparrow/\downarrow}=0$. (b), (d) Real and imaginary parts of the energy differences $\Delta E=(E_+-E_-)$ as a function of k_x and k_y. (c) represents ψ_{+-} as a function of k_x and k_y. Parameters: $\alpha=1$, $\Gamma_{\uparrow}=3$, $\Gamma_{\downarrow}=0$, $\mu=1$, $B=0$.

eigenvalues at zero Zeeman field and at $k_y=0$, see solid blue and dashed red curves. Surprisingly, we observe that both the real and imaginary parts simultaneously merge at finite energy into a single value at special positive and negative momenta. The regime with $\gamma\neq 0$ and $|\gamma|>\alpha|k|$ not only affects the eigenvalues but also the eigenvectors, which can be noticed by inspecting their inner product or overlap $\psi_{+-}=\langle\psi_+||\psi_-\rangle$, $\psi_{\pm}$ is given by equation (5). This overlap is depicted by the green curve in figure 2(a), where we see that it reaches 1 at the special momenta, a situation that can only occur if the eigenvectors are parallel. Although unusual, the behavior of eigenvectors and eigenvalues seen in figure 2(a) is common in NH Hermitian systems. In particular, the spectral degeneracies occurring at the special momenta discussed here signal the emergence of EPs, whose formation can be understood by noting that they occur when the square root in equation (4) vanishes. At zero Zeeman field, the condition for the formation of EPs is given by

$$\alpha^2(k_x^2+k_y^2) - \gamma^2 = 0\,, \tag{6}$$

while at finite Zeeman field we have to change $\alpha k_y \to B + \alpha k_y$. At this EP condition, the eigenvalues and eigenvectors become,

$$E_{\pm}^{\rm EP} = \xi_k - i\Gamma\,,$$
$$\Psi_{\pm}^{\rm EP} = \frac{1}{\sqrt{2}}\begin{pmatrix} 1 \\ \frac{i\gamma}{\alpha(k_y+ik_x)} \end{pmatrix}, \tag{7}$$

where the values of momenta satisfy the condition given by equation (6). Hence, the two eigenvalues (eigenvectors) coalesce at EPs: instead of having two eigenvalues (eigenvectors), only one eigenvalue (eigenvector) remains at EPs, see figure 2(a). For $k_y = 0$, the EP occur at positive and negative momenta given by $\pm k_x^{\rm EP} = \pm(\gamma/\alpha)^2$ at $B = 0$, marking the ends of the cyan region in figure 2(a). Between these two EP points, the eigenvalues have the same real part determined by the quadratic dispersion ξ_k and different imaginary parts determined by $-i\Gamma \pm i\sqrt{\gamma^2 - \alpha^2|k|^2}$, see cyan region in figure 2(a). In relation to the eigenvectors, the fact that both merge into a single eigenvector implies that they are parallel, a situation that has no analog in the Hermitian regime but expected at EPs of NH systems [3]. This effect can be also seen in the inner product (or overlap) between the two eigenvectors $\langle\psi_+||\psi_-\rangle$ in equation (5), where it reaches 1 at the EPs, see green curve in figure 2(a). We remark that for EPs to emerge it is crucial to have eigenvalues with different imaginary parts, which is only achieved when $\Gamma_\uparrow \neq \Gamma_\downarrow$, thus pointing out the necessity of a ferromagnet lead for the NH features discussed in figure 2(a). In passing, we note that having bulk energy lines due to eigenvalues with the same real part resembles the formation of bulk Fermi arcs [26–36], although here they occur at finite real energy in contrast to the common expectation at zero real energy. In this regard, very recently, the definition of bulk Fermi arcs has been generalized to any two eigenvalues with the same real energy [60], suggesting that the bulk energy lines found here might be an example of bulk Fermi arcs. However, the detail properties of this NH bulk effect require a throughout investigation which will be addressed elsewhere.

Furthermore, another property of the EPs determined by the condition in equation (6) is that they occur along a ring defined by $\alpha^2(k_x^2 + k_y^2) = \gamma^2$ at $B = 0$ or by $\alpha^2 k_x^2 + (\alpha k_y + B)^2 = \gamma^2$ at $B \neq 0$. To support this idea, in figures 2(b) and (d) we plot the difference between real and imaginary parts of the eigenvalues, namely, $\mathrm{Re}\Delta E = \mathrm{Re}(E_+ - E_-)$ and $\mathrm{Im}\Delta E = \mathrm{Im}(E_+ - E_-)$, as a function of k_x and k_y. In this case, the blue regions indicate $\mathrm{Re}\Delta E = 0$ and $\mathrm{Im}\Delta E = 0$, with their borders marking the occurrence of rings. To highlight these rings, in figures 2(b) and (d) we also plot the condition given by equation (6) in dashed cyan color. The nature of these rings can be also seen in figure 2(c), where we plot the eigenvector overlap, which acquires 1 exactly along them which implies that the eigenvectors here become parallel as at the EPs discussed previously. This thus demonstrates that the rings seen in figure 2 truly represent bulk exceptional degeneracies of NH 2D Rashba semiconductors and can be referred to as exceptional rings.

To induce the formation of the exceptional degeneracies, or exceptional rings, it is sufficient the interplay between non-Hermiticity and SOC, as clearly seen in equation (6). While this conclusion is already evident in figure 2, to further support it, in figure 3(a) we present $\mathrm{Re}\Delta E$ as a function of the SOC strength α and coupling $\Gamma_\uparrow$ at finite momenta and zero Zeeman field. We obtain that the region with $\mathrm{Re}\Delta E = 0$ increases following a triangular-shaped profile depicted in blue, which is delimited by $\pm\sqrt{\gamma^2/|k|^2}$ indicated by cyan dashed lines. At

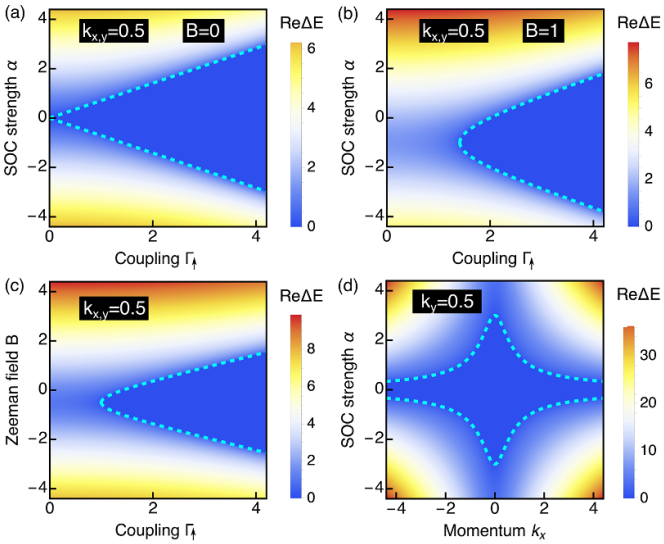

Figure 3. Tunability of exceptional degeneracies in 2D semiconductors with Rashba SOC: (a), (b) Real part of the energy difference $\Delta E = (E_+ - E_-)$ as a function of α and $\Gamma_\uparrow$ at $B = 0$ and $B = 1$. (c), (d) Same quantity as in (a), (b) but as a function of B and $\Gamma_\uparrow$ at $\alpha = 1$ (c), and as a function of α and k_x at $B = 0$ (d). Parameters: $\Gamma_\downarrow = 0$, $\mu = 1$.

fixed momenta, the SOC drives the formation of EPs, requiring lower SOC when non-Hermiticity is small. By fixing only one momentum coordinate, it is also possible to induce EPs, as seen in figure 3(d). Furthermore, another possibility to control the appearance of EPs is by an in-plane Zeeman field along x as considered in figure 1. Thus, in figure 3(b) we show $\mathrm{Re}\Delta E$ as a function of α and $\Gamma_\uparrow$ at finite B, while in figure 3(c) we show $\mathrm{Re}\Delta E$ as a function of B and $\Gamma_\uparrow$. In this case, we identify two relevant features. First, at finite SOC and finite momenta, the non-Hermiticity needed to induce EPs needs to overcome the effect of the Zeeman field B, thus requiring larger non-Hermiticity than in the absence of B (figure 3(b)). Second, at all fixed parameters, the Zeeman field drives the emergence of EPs (figure 3(b)); the EPs here are marked by the cyan curves which correspond to $-\alpha k_y \pm \sqrt{\gamma^2 + \alpha^2 k_x^2}$. In sum, the bulk exceptional degeneracies found in 2D Rashba semiconductors exhibit a high degree of tunability by SOC, momenta, and Zeeman field, which could be relevant for their realization and subsequent observation.

4. Spin projections

Having established the emergence of exceptional degeneracies in the bulk of 2D Rashba semiconductors, now we turn our attention to how the spins here behave under non-Hermiticity. This is motivated by the fact that it is the spin an important quantity for several phenomena in semiconductors, useful for spintronics and topological phenomena. In particular, in this part we focus on the spin expectation values, which here will be referred to as spin projections and are obtained by

$$S_j^\eta = \Psi_\eta^\dagger \sigma_j \Psi_\eta \tag{8}$$

where $\Psi_\eta^\dagger$ is given by equation (5) with $\eta = \pm$ and σ_j the jth spin Pauli matrix. Thus, S_j^η represents the spin projection along j axis associated to $\eta = \pm$. By plugging equation (5) into equation (8), we obtain

$$S_x^\pm = \frac{1}{2\alpha|k|^2}\left[k_x\gamma \pm k_y\sqrt{\alpha^2|k|^2-\gamma^2}\right],$$
$$S_y^\pm = \frac{1}{2\alpha|k|^2}\left[k_y\gamma \mp k_x\sqrt{\alpha^2|k|^2-\gamma^2}\right], \quad (9)$$

for the spin projections along x and y, respectively, while $S_z^\pm = 0$ along z. Note that here $|k|^2 = k_x^2 + k_y^2$ and $\gamma = (\Gamma_\uparrow - \Gamma_\downarrow)/2$ characterizes the amount of non-Hermiticity due to the ferromagnet lead, see equations (1) and (3). As before, the effect of the Zeeman field along x considered in figure 1 can be included by replacing $\alpha k_y \to B + \alpha k_y$. The expressions given by equation (9) are relatively simple and permit us to identify the impact of non-Hermiticity on the spin projections by naked eye. In the Hermitian regime, when $\gamma = 0$, the spin projections reduce to $S_x^\pm = \pm k_y/|k|$ and $S_y^\pm = \mp k_x/|k|$, as expected [52, 53]. Note that $S_{y(x)}^+$ and $S_{y(x)}^-$ change their sign when $k_{x(y)}$ varies from negative to positive values passing through $k_{x(y)} = 0$, see gray and pink curves in figure 4(a) showing the behavior of S_y^+. The sign of $S_{y(x)}^\pm$ remains, however, upon variations of $k_{y(x)}$, as depicted in gray and pink curves in figure 4(c).

For finite non-Hermiticity, characterized by $\gamma \neq 0$, the behavior of the spin projections $S_{x(y)}^\pm$ is highly unusual. A finite γ generates a linear in momentum term proportional to $k_{x(y)}\gamma$ for $S_{x(y)}$ and renormalizes the Hermitian component with $\sqrt{\alpha^2|k|^2-\gamma^2}$, see first and second terms in equation (9). Both terms reveal a unique effect of non-Hermiticity. The first part of $S_{x(y)}^\pm$, proportional to $k_{x(y)}\gamma$, is always real and appears along the same direction of the spin projection, in contrast to the Hermitian contribution where $S_{x(y)}^\pm$ is only finite along $y(x)$. The second part of $S_{x(y)}^\pm$ is real for $|\alpha||k| > |\gamma|$, which then adds up to the first part, but becomes imaginary for $|\alpha||k| < |\gamma|$. Thus, the appearance of an imaginary part in the spin projections for $|\alpha||k| < |\gamma|$ can be interpreted as a signal of their lifetime, which becomes highly anisotropic in momentum space. At $\alpha^2|k|^2 - \gamma^2 = 0$, the second term in equation (9) vanish and the spin projections $S_j^\pm$ coalesce, namely, they merge into a single value that is given by

$$S_{x(y)}^{\pm,\mathrm{EP}} = \frac{k_{x(y)}}{2|k|^2}. \quad (10)$$

Interestingly, the condition $\alpha^2|k|^2 - \gamma^2 = 0$, which leads to this spin projection coalescence, is the same condition that determines the formation of exceptional degeneracies discussed in previous section, see equation (6). Thus, the coalescence effect of $S_j^\pm$ can be seen as unique NH effect without analog in Hermitian systems. We also note that along the lines connecting these exceptional degeneracies, which correspond to energy lines that resemble bulk Fermi arcs, the spin projections acquire a finite imaginary part with a natural physical interpretation as discussed in previous paragraph.

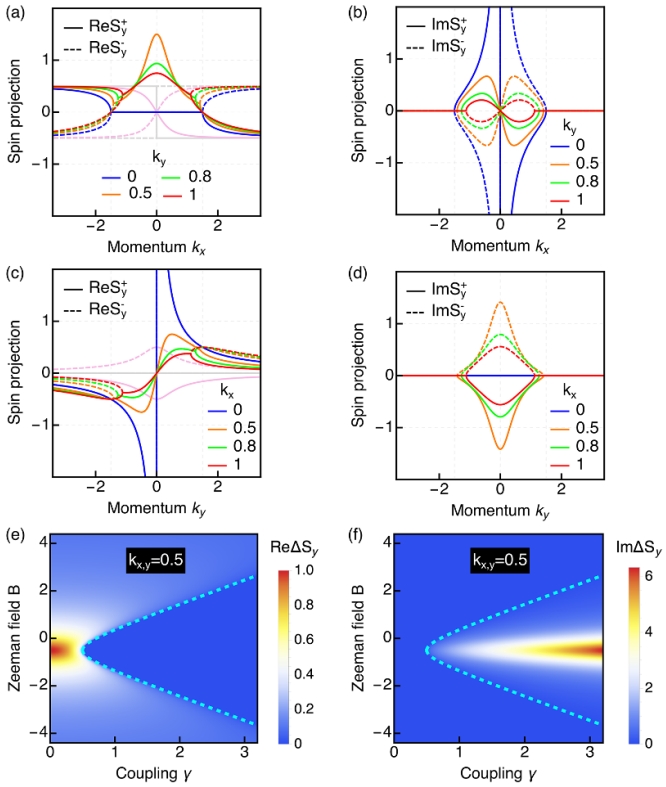

Figure 4. Spin projection along y, $S_y^\pm$: (a), (b) Real (Re) and imaginary (Im) parts of the spin projection, Re$[S_y^\pm]$ and Im$[S_y^\pm]$, as a function of k_x for distinct values of k_y at $B = 0$ where solid (dashed) curves correspond to the spin projections obtained with ψ_+ (ψ_-). Also, light gray (brown) curves showing a sharp (smooth) transition across $k_x = 0$ correspond to $\Gamma_{\uparrow,\downarrow} = 0$ and $k_y = 0$ ($k_y = 0.5$). (c), (d) Same as (a), (b) but now as a function of k_y at distinct values of k_x. (e), (f) Real and imaginary parts of the spin-projection differences $\Delta S_y = S_y^- - S_y^+$ as a function of B and γ at finite momenta $k_{x,y} = 0.5$. The dashed cyan lines indicate the regimes where exceptional points occur, which then mark the ends of ReΔS$_y = 0$ (uniform blue region). Parameters: $\Gamma_\uparrow = 3$, $\alpha = 1$, $\Gamma_\downarrow = 0$, $\mu = 1$.

In order to gain visual understanding of the spin projection coalescence, in figure 4 we plot the real and imaginary parts of $S_y^\pm$ as a function of momenta (a–d) and in the $B - \gamma$ plane (e,f). At $k_y = 0$, the real part of the spin projections $S_y^\pm$ vanishes along a line of k_x and the ends of such line mark the EP momenta obtained from equation (6) and given by $|k_x^{\mathrm{EP}}| = |\gamma|/|\alpha|$, see solid and dashed blue curves in figure 4(a); see also equations (9) and (10). The imaginary part of $S_y^\pm$ undergoes a coalescence effect as well at the EP momenta $\pm k_x^{\mathrm{EP}}$ but acquires large values between them and vanish at $k_x = 0$ (figure 4(b)). For $k_y > 0$, the coalescence effect persists, with smaller imaginary parts, but the real part does not vanish anymore and, instead, develops a maximum at $k_x = 0$ favoring a large positive spin projection along y, see equations (9) and (10). For $k_y < 0$, the spin projection $S_y^\pm$ has instead a minimum at $k_x = 0$, favoring a large negative spin projection along y. The coalescence of spin projections is also observed in figures 4(c) and (d), where we plot the real and imaginary parts of $S_y^\pm$ as a function of k_y at fixed values of k_x. At $k_x = 0$, no EP transition is observed in $S_y^\pm$ because the square root term

that gives rise to EPs is multiplied by zero and hence vanishes, see blue curves in figures 4(c) and (d) and also equation (9). However, for finite k_x, the spin projections develop a clear EP transition, revealing that their coalescence is a highly tunable NH bulk effect.

The spin projection coalescence discussed above requires finite momenta, Rashba SOC, and non-Hermiticity, a combination of ingredients inherent to NH Rashba semiconductors. Furthermore, it is also possible to tune and control the spin projections by an in-plane Zeeman field B, e.g. along x as sketched in figure 1, see also discussions below equations (2) and (9). To support this idea, in figures 4(e) and (f) we present the Re and the Im parts of the difference between spin projection along y, $\mathrm{Re}\Delta S_y = \mathrm{Re}(S_y^- - S_{y)}^+$ and $\mathrm{Im}\Delta S_y = \mathrm{Im}(S_y^- - S_{y)}^+$, at fixed $k_{x,y}$ as a function of B and γ. Here, the blue regions indicate $\mathrm{Re}\Delta S_y = 0$ and $\mathrm{Im}\Delta S_y = 0$ and their borders show the exceptional degeneracies, indicated in cyan dashed curves. At fixed non-Hermiticity (γ), the Zeeman field B induces the coalescence of spin projections $S_y^{\pm}$ at EPs, which requires small (large) B for weak (strong) non-Hermiticity. Therefore, Zeeman fields offer another possibility for tuning and controlling the spin-projection coalescence at exceptional degeneracies in 2D Rashba semiconductors.

5. Spectral signatures

In this part we explore the spectral function as a potential way for detecting EPs in NH Rashba semiconductors, which can be measured by tools such as ARPES [64–69]. The spectral function can be obtained as $A(k,\omega) = -\mathrm{Im}\,\mathrm{Tr}(G^r - G^a)$, where $G^r = (\omega - H_{\mathrm{eff}})^{-1}$ and $G^a = (G^r)^\dagger$ are the retarded and advanced Green's functions, respectively [70, 71]. The expressions for $G^{r(a)}$ are not complicated, which allows us to write down the spectral function as

$$A(\omega,k) = -2\mathrm{Im}\left[\frac{1}{\omega - E_-(k)} + \frac{1}{\omega - E_+(k)}\right], \qquad (11)$$

where $E_\pm(k)$ are given by equation (4). Although this expression already reveals the behavior of the spectral function in our system, it is useful to write it as

$$A(\omega,k) = -2\mathrm{Im}\sum_{i=\pm}\left[\frac{\omega - \mathrm{Re}E_i}{D(\omega,E_i)} - i\frac{\mathrm{Im}E_i}{D(\omega,E_i)}\right], \qquad (12)$$

with $D(\omega,E_i) = (\omega - \mathrm{Re}E_i)^2 + (\mathrm{Im}E_i)^2$. Now, we clearly see that the spectral function in our system is a sum of two Lorentzians centered at $\omega = \mathrm{Re}E_\pm$ with their height and width characterized by $\mathrm{Im}E_\pm$. It is thus evident in equation (12) that, at the EPs and at momenta between them where eigenvalues merge, instead of two Lorentzian resonances we only have one.

The behavior of the spectral function can be further visualized in figure 5(a), where we plot A as a function of ω and k_x at $k_y = 0$, $B = 0.5$; the real and imaginary parts of the eigenvalues are shown in dashed blue and dashed red curves. We also plot line cuts in figure 5(b) for distinct k-values spanning the momenta at which EP occur (yellow curves), and

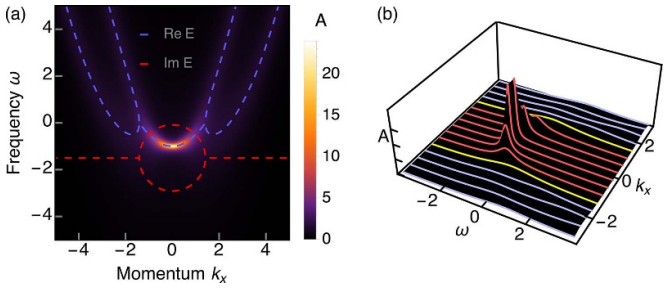

Figure 5. (a) Spectral function $A(\omega,k)$ as a function of ω and momentum k_x. Here, also the real and imaginary parts of the eigenvalues are shown in dashed blue and dashed red curves, respectively. (b) Line cuts of A with EPs (yellow), region between EPs (red), and region beyond (light blue). Parameters: $\Gamma_\uparrow = 3$, $k_y = 0$, $\alpha = 1$, $\Gamma_\downarrow = 0$, $\mu = 1$, $B = 0.5$.

momenta between EPs (red curves). The immediate observation is that A develops high intensity regions for a line of momenta bounded by the EP momenta, revealing both the position of EPs and the formation of the finite real energy Fermi arcs. At the EPs, marked by yellow lines in figure 5(b), the spectral function undergoes a transition along k from having two resonances to having a single resonance centered at $\mathrm{Re}E_{1,2} \equiv \xi_k$, see also equation (12). For momenta between the EPs, the real parts stick together $\mathrm{Re}E_{1,2} \equiv \xi_k$ and a single resonance remains all over these momenta, see red curves. Interestingly, the resonances between the EPs acquire very large values which could be also useful for identifying the bulk Fermi arc at real energies found here. Before ending this part, we would like to mention that the length of the high intensity region seen in figure 5(a) along k, which is the length of the arc, not only permits to estimate the EP momenta but it also allows to identify the amount of non-Hermiticity γ according to equation (6). Alternatively, this feature could provide a way to assess the strength of SOC α, provided γ is known as dictated by equation (6). In sum, the spectral function reveals unique features of EPs and offers a powerful route for their detection.

6. Conclusions

We have demonstrated that the interplay between non-Hermiticity and Rashba SOC in semiconductors gives rise to the emergence of stable and highly tunable bulk exceptional degeneracies. We have found that these degeneracies form rings in two-dimensional momentum space and signal the ends of lines forming due to the coalescence of eigenvalues at finite real energy. Interestingly, the lines at finite real energies have the appearance of bulk Fermi arcs but now at finite energies, suggesting new possibilities for NH bulk phenomena [60], whose detail properties, however, deserve a proper investigation and will be addressed in a future study. We have also shown that the exceptional degeneracies and bulk Fermi arcs can be controlled by an in-plane Zeeman field, albeit larger non-Hermiticity values are then needed. Furthermore, we have discovered that the spin projections coalesce at the exceptional degeneracies and can easily achieve higher values than in the

Hermitian regime. We also demonstrate that the exceptional degeneracies induce large spectral features along momenta connecting them, unique features that can be directly detected by ARPES. Taken together, the results presented here put semiconductors with Rashba SOC as an interesting arena for the realization of highly tunable NH bulk phenomena.

We also note that there is reasonable evidence suggesting that the system studied here as well as the main findings are within experimental reach. In fact, very similar systems as studied here have already been fabricated, including semiconductors with SOC made of InAs [72–77] or InSb [78–82] and ferromagnets producing sizeable Zeeman fields [83–89]. The coupling between ferromagnet and semiconductor, here characterized by Γ_σ, can be controlled by an appropriate manipulation of both the spin-dependent density of states in the lead and the tunneling between lead and semiconductor. While the Zeeman field of the ferromagnet enables a distinct density of states for different spins, thus producing different couplings Γ_σ, the overall strength of such couplings can be tuned by inserting a normal potential barrier of finite thickness between the semiconductor and ferromagnet lead, e.g. by using a few nm thick InGaAs layer [73]. We have estimated that, using $\mu_{\rm L} = 1$ meV, $t_z = 2$ meV, a ferromagnet with a Zeeman field of the order of 3meV would be necessary to achieve the conditions of distinct couplings of $\Gamma_\uparrow = 0.4$ meV and $\Gamma_\downarrow = 0$, thus giving $\gamma = 0.2$ meV. Under these conditions and considering $k_y = 0$ and $\alpha = 20$ meVnm, which is in the range of the SOC in InAs and InSb, we obtain that the EP conditions are satisfied for $k_x \approx 0.7\,{\rm nm}^{-1}$ or $k_x^{-1} = 150$ nm, which is clearly in the range of reasonable length scales in these systems, such as the length scale related to SOC [55]. We can thus conclude that, despite the possible challenges, there already exist experiments suggesting that the NH semiconductor and the EPs studied here represent a feasible idea.

Data availability statement

All data that support the findings of this study are included within the article (and any supplementary files).

Acknowledgments

We thank A M Black-Schaffer and P Oppeneer for useful discussions. We acknowledge financial support from the Swedish Research Council (Vetenskapsråd Grant No. 2021-04121), the Göran Gustafsson Foundation (Grant No. 2216), the Scandinavia-Japan Sasakawa Foundation (Grant No. GA22-SWE-0028), the Royal Swedish Academy of Sciences (Grant No. PH2022-0003), and the C F Liljewalchs stipendiestiftelse Foundation.

Appendix. Derivation of the self-energy

In this part we show how the retarded self-energy Σ^r given by equation (3) is derived. At this point, we remind that our open system is modeled by an effective Hamiltonian $H_{\rm eff}$ given by equation (1) that contains the Hamiltonian $H_{\rm R}$ of an isolated 2D semiconductor and a self-energy due to its coupling to a semi-infinite ferromagnetic lead, modeled by the Hamiltonian $H_{\rm L}$. Thus, the open system we study consists of a 2D junction along z: the closed system $H_{\rm R}$ corresponds to a 2D semiconductor, which can be seen of as having one site along z, while the ferromagnetic lead is semi-infinite along z for negative z, see figure 1.

As already pointed out in section 2, the self-energy Σ^r depends on frequency under general circumstances and can be obtained as $\Sigma^r(\omega) = V^\dagger g^r_{\rm L}(\omega) V$, where $g^r_{\rm L}(\omega) = (\omega - H_{\rm L})^{-1}$ is the retarded Green's function of the semi-infinite lead and V is the hopping matrix between the system and the lead. Because V is only finite between the nearest neighbor sites of the ferromagnet lead and the Rashba semiconductor, it is possible to project the self-energy onto $H_{\rm R}$, which reads

$$\Sigma^r_{1_{\rm R}1_{\rm R}}(\omega) = \langle 1_{\rm R}|V^\dagger|1_{\rm L}\rangle\langle 1_{\rm L}|g^r_{\rm L}(\omega)|1_{\rm L}\rangle\langle 1_{\rm L}|V|1_{\rm R}\rangle\,, \qquad \text{(A.1)}$$

where $1_{\rm L}$ denotes the first site of the lead, closest to the semiconductor, while $1_{\rm R}$ denotes the only site in the Rashba semiconductor along the z-direction. We also set $\langle 1_{\rm L}|V|1_{\rm R}\rangle \equiv V_{1_{\rm L}1_{\rm R}} = -t'\sigma_0$, where t' is the hopping amplitude between sites $1_{\rm L}$ in the lead and site $1_{\rm R}$ in the semiconductor. It is interesting to notice that equation (A.1) implies that it is only required the Green's function of the lead at site $1_{\rm L}$, which is the surface lead Green's function.

To find the surface lead Green's function, it is important to remark that as a result of the lead being semi-infinite along the negative z-direction, it contains an infinite number of sites in this direction, with the Hamiltonian for each site ($i_{\rm L}$) given by the on-site terms as $[H_{\rm L}]_{i_{\rm L}i_{\rm L}} = \xi^{\rm L}_k\sigma_0 + B_{\rm L}\sigma_z$, where $\xi^{\rm L}_k = \hbar^2k^2/2m - \mu_{\rm L}$ is the kinetic term in the lead, with $k = (k_x, k_y)$, and chemical potential $\mu_{\rm L}$. Also, $B_{\rm L}$ is the Zeeman energy, which appears because the lead is ferromagnetic, but it might be also due to an external magnetic field. Thus, to find the lead Green's function, it is important to take into account that $H_{\rm L}$ is an infinite matrix. Then, by using a recursive approach [61], we find $\langle 1_{\rm L}|g^r_{\rm L}(\omega)|1_{\rm L}\rangle = {\rm diag}(g^r_{\uparrow\uparrow}, g^r_{\downarrow\downarrow})$, with the diagonal entries given by

$$g^r_{\sigma\sigma}(\omega) = \frac{1}{|t_z|}\left[\frac{\omega-\epsilon_\sigma}{2|t_z|} - i\sqrt{1-\left(\frac{\omega-\epsilon_\sigma}{2|t_z|}\right)^2}\right]. \qquad \text{(A.2)}$$

for $|(\omega - \epsilon^{e(h)}_\sigma)/2|t_z|| < 1$. Here, $\epsilon_\sigma = \xi^{\rm L}_k + \sigma B_{\rm L}$. We can then write the self-energy in spin space as

$$\Sigma^r_{1_{\rm R}1_{\rm R}} = \begin{pmatrix} t'^2 g^r_{\uparrow\uparrow} & 0 \\ 0 & t'^2 g^r_{\downarrow\downarrow}\end{pmatrix}, \qquad \text{(A.3)}$$

which involves real and imaginary terms due to the imaginary part of the lead Green's function. While under general circumstances, both real and imaginary parts impact the Hamiltonian of the 2D Rashba semiconductor $H_{\rm R}$, only the imaginary term gives rise to NH physics.

Here, we are here interested in the effect of the NH part of the self-energy and for this purpose we it is useful to carry out some approximations. First, we consider $|(\omega - \epsilon^{e(h)}_\sigma)/(2t_z)| \ll |(\mu_{\rm L} - \sigma B)/(2t_z)| < 1$, which can be seen to be a sort of wide

band limit widely used in quantum transport [48, 90] that permits us to neglect the dependence on both frequency and momentum in the lead Green's function $g^r_{\rm L}$. Notice that we still assume values of B and $\mu_{\rm L}$ to be large enough such that $g^r_{\rm L}$ develops different imaginary terms for different spins. Second, we neglect the real part of the self-energy as it only introduces shifts into the semiconductor Hamiltonian $H_{\rm R}$: we only keep the imaginary term of the self-energy because it renders NH the effective Hamiltonian $H_{\rm eff}$ of the total system. The possible energy shifts due to the real part of the self-energy can be incorporated by an appropriate renormalization of the semiconductor Hamiltonian by spanning over relevant parameter regimes. We can thus safely neglect the frequency and momentum dependence of the self-energy and also its real part, enabling us to only focus on the imaginary component for inducing NH physics and EPs. Hence, we can approximate the self-energy $\Sigma^r_{1_{\rm R}1_{\rm R}}$ in equation (A.3) as

$$\Sigma^r(\omega=0) = -i\Gamma\sigma_0 - i\gamma\sigma_z\,, \tag{A.4}$$

where $\Gamma = (\Gamma_\uparrow + \Gamma_\downarrow)/2$ and $\gamma = (\Gamma_\uparrow - \Gamma_\downarrow)/2$. Here we have defined $\Gamma_\sigma = \pi|t'|^2\rho^\sigma_{\rm L}$, where $\rho^{\uparrow(\downarrow)}_{\rm L} = [1/(t_z\pi)]\sqrt{1-[(\mu_{\rm L}\mp B)/(2t_z)]^2}$ is the spin-polarized surface density of states of the lead. Equation (A.4) is presented as equation (3) of the main text, where its impact for inducing EPs is further discussed.

ORCID iD

Jorge Cayao https://orcid.org/0000-0001-6037-6243

References

[1] El-Ganainy R, Makris K G, Khajavikhan M, Musslimani Z H, Rotter S and Christodoulides D N 2018 Non-hermitian physics and pt symmetry *Nat. Phys.* **14** 11–19

[2] Özdemir S K, Rotter S, Nori F and Yang L 2019 Parity–time symmetry and exceptional points in photonics *Nat. Mater.* **18** 783–98

[3] Bergholtz E J, Carl Budich J C and Kunst F K 2021 Exceptional topology of non-hermitian systems *Rev. Mod. Phys.* **93** 015005

[4] Ashida Y, Gong Z and Ueda M 2020 Non-hermitian physics *Adv. Phys.* **69** 249–435

[5] Parto M, Liu Y G N, Bahari B, Khajavikhan M and Christodoulides D N 2020 Non-hermitian and topological photonics: optics at an exceptional point *Nanophotonics* **10** 403–23

[6] Wiersig J 2020 Review of exceptional point-based sensors *Photon. Res.* **8** 1457–67

[7] Ding K, Fang C and Ma G 2022 Non-hermitian topology and exceptional-point geometries *Nat. Rev. Phys.* **4** 745–60

[8] Gong Z, Ashida Y, Kawabata K, Takasan K, Higashikawa S and Ueda M 2018 Topological phases of non-hermitian systems *Phys. Rev.* X **8** 031079

[9] Zhou H and Yeon Lee J Y 2019 Periodic table for topological bands with non-hermitian symmetries *Phys. Rev.* B **99** 235112

[10] Kawabata K, Shiozaki K, Ueda M and Sato M 2019 Symmetry and topology in non-hermitian physics *Phys. Rev.* X **9** 041015

[11] Kato T 1966 *Perturbation Theory of Linear Operators* (New York: Springer)

[12] Heiss W D 2004 Exceptional points–their universal occurrence and their physical significance *Czechoslov. J. Phys.* **54** 1091–9

[13] Berry M V 2004 Physics of nonhermitian degeneracies *Czechoslov. J. Phys.* **54** 1039–47

[14] Heiss W D 2012 The physics of exceptional points *J. Phys. A: Math. Theor.* **45** 444016

[15] Dembowski C, Gräf H-D, Harney H L, Heine A, Heiss W D, Rehfeld H and Richter A 2001 Experimental observation of the topological structure of exceptional points *Phys. Rev. Lett.* **86** 787–90

[16] Lee S-B, Yang J, Moon S, Lee S-Y, Shim J-B, Wook Kim S W, Lee J-H and An K 2009 Observation of an exceptional point in a chaotic optical microcavity *Phys. Rev. Lett.* **103** 134101

[17] Choi Y, Kang S, Lim S, Kim W, Kim J-R, Lee J-H and An K 2010 Quasieigenstate coalescence in an atom-cavity quantum composite *Phys. Rev. Lett.* **104** 153601

[18] Gao T *et al* 2015 Observation of non-hermitian degeneracies in a chaotic exciton-polariton billiard *Nature* **526** 554–8

[19] Doppler Jorg, Mailybaev A A, Böhm J, Kuhl U, Girschik A, Libisch F, Milburn T J, Rabl P, Moiseyev N and Rotter S 2016 Dynamically encircling an exceptional point for asymmetric mode switching *Nature* **537** 76–79

[20] Yoshida T, Peters R, Kawakami N and Hatsugai Y 2019 Symmetry-protected exceptional rings in two-dimensional correlated systems with chiral symmetry *Phys. Rev.* B **99** 121101

[21] Arouca R, Cayao J and Black-Schaffer A M 2022 Exceptionally enhanced topological superconductivity (arXiv:2206.15324)

[22] Hodaei H, Hassan A U, Wittek S, Garcia-Gracia H, El-Ganainy R, Christodoulides D N and Khajavikhan M 2017 Enhanced sensitivity at higher-order exceptional points *Nature* **548** 187–91

[23] Chen W, Kaya Özdemir S, Zhao G, Wiersig J and Yang L 2017 Exceptional points enhance sensing in an optical microcavity *Nature* **548** 192–6

[24] Peng B, Kaya Özdemir Şahin, Liertzer M, Chen W, Kramer J, Yılmaz H, Wiersig J, Rotter S and Yang L 2016 Chiral modes and directional lasing at exceptional points *Proc. Natl Acad. Sci. USA* **113** 6845–50

[25] Longhi S and Feng L 2017 Unidirectional lasing in semiconductor microring lasers at an exceptional point *Photon. Res.* **5** B1–B6

[26] Kozii V and Liang F 2017 Non-hermitian topological theory of finite-lifetime quasiparticles: prediction of bulk fermi arc due to exceptional point (arXiv:1708.05841)

[27] Ghatak A and Das T 2018 Theory of superconductivity with non-hermitian and parity-time reversal symmetric cooper pairing symmetry *Phys. Rev.* B **97** 014512

[28] Yoshida T, Peters R and Kawakami N 2018 Non-hermitian perspective of the band structure in heavy-fermion systems *Phys. Rev.* B **98** 035141

[29] Okugawa R and Yokoyama T 2019 Topological exceptional surfaces in non-hermitian systems with parity-time and parity-particle-hole symmetries *Phys. Rev.* B **99** 041202

[30] Kawabata K, Bessho T and Sato M 2019 Classification of exceptional points and non-hermitian topological semimetals *Phys. Rev. Lett.* **123** 066405

[31] Yamamoto K, Nakagawa M, Adachi K, Takasan K, Ueda M and Kawakami N 2019 Theory of non-hermitian fermionic superfluidity with a complex-valued interaction *Phys. Rev. Lett.* **123** 123601

[32] Zhou H, Peng C, Yoon Y, Hsu C W, Nelson K A, Fu L, Joannopoulos J D, Soljačić M and Zhen B 2018 Observation of bulk fermi arc and polarization half charge from paired exceptional points *Science* **359** 1009–12

[33] Bessho T, Kawabata K and Sato M 2019 *Topological Classificaton of Non-Hermitian Gapless Phases: Exceptional Points and Bulk Fermi Arcs* (Physical Society of Japan) ch 30, p 011098

[34] Nagai Y, Qi Y, Isobe H, Kozii V and Fu L 2020 Dmft reveals the non-hermitian topology and fermi arcs in heavy-fermion systems *Phys. Rev. Lett.* **125** 227204

[35] Mandal I and Bergholtz E J 2021 Symmetry and higher-order exceptional points *Phys. Rev. Lett.* **127** 186601

[36] Delplace P, Yoshida T and Hatsugai Y 2021 Symmetry-protected multifold exceptional points and their topological characterization *Phys. Rev. Lett.* **127** 186602

[37] Yoshida T, Peters R, Kawakami N and Hatsugai Y 2020 Exceptional band touching for strongly correlated systems in equilibrium *Prog. Theor. Exp. Phys.* **2020** 12A109

[38] Rausch R, Peters R and Yoshida T 2021 Exceptional points in the one-dimensional hubbard model *New J. Phys.* **23** 013011

[39] Pikulin D I and Nazarov Y V 2012 Topological properties of superconducting junctions *JETP Lett.* **94** 693–7

[40] Pikulin D I and Nazarov Y V 2013 Two types of topological transitions in finite majorana wires *Phys. Rev.* B **87** 235421

[41] San-Jose P, Cayao J, Prada E and Aguado Ron 2016 Majorana bound states from exceptional points in non-topological superconductors *Sci. Rep.* **6** 21427

[42] Avila J, Pe naranda F, Prada E, San-Jose P and Aguado R 2019 Non-hermitian topology as a unifying framework for the andreev versus majorana states controversy *Commun. Phys.* **2** 133

[43] Philip T M, Hirsbrunner M R and Gilbert M J 2018 Loss of hall conductivity quantization in a non-hermitian quantum anomalous hall insulator *Phys. Rev.* B **98** 155430

[44] Chen Y and Zhai H 2018 Hall conductance of a non-hermitian chern insulator *Phys. Rev.* B **98** 245130

[45] Bergholtz E J and Carl Budich J C 2019 Non-hermitian weyl physics in topological insulator ferromagnet junctions *Phys. Rev. Res.* **1** 012003

[46] Cayao J and Black-Schaffer A M 2022 Exceptional odd-frequency pairing in non-hermitian superconducting systems *Phys. Rev.* B **105** 094502

[47] Cayao J and Annica M B-S 2022 Bulk bogoliubov fermi arcs in non-hermitian superconducting systems (arXiv:2208.05372)

[48] Datta S 1997 *Electronic Transport in Mesoscopic Systems* (Cambridge: Cambridge University Press)

[49] Dresselhaus G 1955 Spin-orbit coupling effects in zinc blende structures *Phys. Rev.* **100** 580–6

[50] Rashba E I 1960 Properties of semiconductors with an extremum loop *Sov. Phys. Solid. State* **2** 1109–22

[51] Bychkov Y A and Rashba E I 1984 Properties of a 2d electron gas with lifted spectral degeneracy *Sov. Phys. JETP* **39** 78

[52] Winkler R 2003 *Spin-Orbit Coupling Effects in Two-Dimensional Electron and Hole Systems* vol 191 (Berlin: Springer)

[53] Chen J, Wu K, Hu W and Yang J 2021 Spin–orbit coupling in 2D semiconductors: a theoretical perspective *J. Phys. Chem. Lett.* **12** 12256–68

[54] Manchon A, Cheol Koo H C, Junsaku Nitta J, Frolov S M and Duine R A 2015 New perspectives for rashba spin–orbit coupling *Nat. Mater.* **14** 871–82

[55] Lutchyn R M, Bakkers E P A M, Kouwenhoven L P, Krogstrup P, Marcus C M and Oreg Y 2018 Majorana zero modes in superconductor-semiconductor heterostructures *Nat. Rev. Mater.* **3** 52

[56] Prada E, San-Jose P, de Moor M W A, Geresdi A, Lee E J H, Klinovaja J, Loss D, Nygård J, Aguado Ron and Kouwenhoven L P 2020 From Andreev to Majorana bound states in hybrid superconductor–semiconductor nanowires *Nat. Rev. Phys.* **2** 575–94

[57] Flensberg K, von Oppen F and Stern A 2021 Engineered platforms for topological superconductivity and majorana zero modes *Nat. Rev. Mater.* **6** 944–58

[58] Sestoft J E *et al* 2018 Engineering hybrid epitaxial inassb/al nanowires for stronger topological protection *Phys. Rev. Mater.* **2** 044202

[59] Kammhuber J *et al* 2017 Conductance through a helical state in an indium antimonide nanowire *Nat. Commun.* **8** 478

[60] Haiping H, Sun S and Chen S 2022 Knot topology of exceptional point and non-hermitian no-go theorem *Phys. Rev. Res.* **4** L022064

[61] Cayao J, Prada E, San-Jose P and Aguado Ron 2015 Sns junctions in nanowires with spin-orbit coupling: role of confinement and helicity on the subgap spectrum *Phys. Rev.* B **91** 024514

[62] Oshima D, Taguchi K and Tanaka Y 2018 Tunneling conductance in two-dimensional junctions between a normal metal and a ferromagnetic rashba metal *J. Phys. Soc. Japan* **87** 034710

[63] Oshima D, Taguchi K and Tanaka Y 2019 Unconventional gate voltage dependence of the charge conductance caused by spin-splitting fermi surface by rashba-type spin-orbit coupling *Physica E: Low Dimens. Syst. Nanostruct.* **114** 113615

[64] Hüfner S 2013 *Photoelectron Spectroscopy: Principles and Applications* (Berlin: Springer Science and Business Media)

[65] Baiqing Lv, Qian T and Ding H 2019 Angle-resolved photoemission spectroscopy and its application to topological materials *Nat. Rev. Phys.* **1** 609–26

[66] Yu T, Matt C E, Bisti F, Wang X, Schmitt T, Chang J, Eisaki H, Feng D and Strocov V N 2020 The relevance of arpes to high-t c superconductivity in cuprates *npj Quantum Mater.* **5** 46

[67] Shimojima T, Okazaki K and Shin S 2015 Low-temperature and high-energy-resolution laser photoemission spectroscopy *J. Phys. Soc. Japan* **84** 072001

[68] Sobota J A, He Y and Shen Z-X 2021 Angle-resolved photoemission studies of quantum materials *Rev. Mod. Phys.* **93** 025006

[69] Kornich V and Trauzettel Born 2022 Signature of $\mathcal{PT}$-symmetric non-hermitian superconductivity in angle-resolved photoelectron fluctuation spectroscopy *Phys. Rev. Res.* **4** L022018

[70] Mahan G D 2013 *Many-Particle Physics* (New York: Springer Science and Business Media)

[71] Zagoskin A 2014 *Quantum Theory of Many-Body Systems: Techniques and Applications* (Berlin: Springer)

[72] Kjaergaard M *et al* 2016 Quantized conductance doubling and hard gap in a two-dimensional semiconductor-superconductor heterostructure *Nat. Commun.* **7** 12841

[73] Shabani J *et al* 2016 Two-dimensional epitaxial superconductor-semiconductor heterostructures: a platform for topological superconducting networks *Phys. Rev.* B **93** 155402

[74] Suominen H J, Kjaergaard M, Hamilton A R, Shabani J, Palmstrßm C J, Marcus C M and Nichele F 2017 Zero-energy modes from coalescing Andreev states in a two-dimensional semiconductor-superconductor hybrid platform *Phys. Rev. Lett.* **119** 176805

[75] Bßttcher C G L, Nichele F, Kjaergaard M, Suominen H J, Shabani J, Palmstrßm C J and Marcus C M 2018 Superconducting, insulating and anomalous metallic regimes in a gated two-dimensional semiconductor–superconductor array *Nat. Phys.* **14** 1138–44

[76] Fornieri A *et al* 2019 Evidence of topological superconductivity in planar josephson junctions *Nature* **569** 89–92

[77] O'Connell Yuan J, Wickramasinghe K S, Strickland W M, Dartiailh M C, Sardashti K, Hatefipour M and Shabani J 2021 Epitaxial superconductor-semiconductor two-dimensional systems for superconducting quantum circuits *J. Vac. Sci. Technol. A: Vac. Surf.* **39** 033407
[78] Gazibegovic S, Badawy G, Buckers T L J, Leubner P, Shen J, de Vries F K, Koelling S, Kouwenhoven L P, Verheijen M A and Bakkers E P A M 2019 Bottom-up grown 2D insb nanostructures *Adv. Mater.* **31** 1808181
[79] Ke C T *et al* 2019 Ballistic superconductivity and tunable π–junctions in insb quantum wells *Nat. Commun.* **10** 3764
[80] Xue J, Chen Y, Pan D, Wang J-Y, Zhao J, Huang S and Xu H Q 2019 Gate defined quantum dot realized in a single crystalline insb nanosheet *Appl. Phys. Lett.* **114** 023108
[81] Lei Z, Lehner C A, Cheah E, Karalic M, Mittag C, Alt L, Scharnetzky J, Wegscheider W, Ihn T and Ensslin K 2019 Quantum transport in high-quality shallow insb quantum wells *Appl. Phys. Lett.* **115** 012101
[82] Chen Y, Huang S, Pan D, Xue J, Zhang Li, Zhao J and Xu H Q 2021 Strong and tunable spin–orbit interaction in a single crystalline insb nanosheet *npj 2D Mater. Appl.* **5** 3
[83] Katmis F *et al* 2016 A high-temperature ferromagnetic topological insulating phase by proximity coupling *Nature* **533** 513–6
[84] Liu Y *et al* 2019 Semiconductor–ferromagnetic insulator–superconductor nanowires: stray field and exchange field *Nano Lett.* **20** 456–62
[85] Yang Z, Heischmidt B, Gazibegovic S, Badawy G, Car D, Crowell P A, Bakkers E P A M and Pribiag V S 2020 Spin transport in ferromagnet-insb nanowire quantum devices *Nano Lett.* **20** 3232–9
[86] Vaitiekėnas S, Liu Y, Krogstrup P and Marcus C M 2021 Zero-bias peaks at zero magnetic field in ferromagnetic hybrid nanowires *Nat. Phys.* **17** 43–47
[87] Escribano S D, Maiani A, Leijnse M, Flensberg K, Oreg Y, Levy Yeyati A, Prada E and Seoane Souto R 2022 Semiconductor-ferromagnet-superconductor planar heterostructures for 1d topological superconductivity *npj Quantum Mater.* **7** 81
[88] Vaitiekėnas S, Seoane Souto R, Liu Y, Krogstrup P, Flensberg K, Leijnse M and Marcus C M 2022 Evidence for spin-polarized bound states in semiconductor–superconductor–ferromagnetic-insulator islands *Phys. Rev.* B **105** L041304
[89] Razmadze D, Seoane Souto R, Galletti L, Maiani A, Liu Y, Krogstrup P, Schrade C, Gyenis A, Marcus C M and Vaitiekėnas S 2023 Supercurrent reversal in ferromagnetic hybrid nanowire josephson junctions *Phys. Rev.* B **107** L081301
[90] Ryndyk D A, Gutiérrez R, Song B and Cuniberti G 2009 *Green Function Techniques in the Treatment of Quantum Transport at the Molecular Scale* (Berlin: Springer) pp 213–335